J. Fluid Mech. (2021), *vol*. 926, R3, doi:10.1017/jfm.2021.745

Time-dependent measurements of length and area of the contact line in contact-boiling regime

Mohammad Khavari[1,2] **and Tuan Tran**[3,†]

[1]Faculty of Technology, Design and Environment, Oxford Brookes University, Oxford OX33 1HX, UK

[2]Department of Materials, University of Oxford, Parks Road, Oxford OX1 3PH, UK

[3]School of Mechanical and Aerospace Engineering, Nanyang Technological University, 50 Nanyang Avenue, 639798, Republic of Singapore

(Received 10 May 2021; revised 29 June 2021; accepted 9 August 2021)

During the impact of a liquid droplet on a sufficiently heated surface, bubble nucleation reduces the contact area between the liquid and the solid surface. Using high-speed imaging combined with total internal reflection, we measure and report how the contact area decreases with time for a wide range of surface temperatures and impact velocities. We also reveal how formation of the observed fingering patterns contributes to a substantial increase in the total length of the contact line surrounding the contact area.

Key words: boiling, drops, bubble dynamics

1. Introduction

Evaporation of liquid droplets impacting on a sufficiently heated solid surface occurs in numerous industrial applications, such as thermal spray (Davis *et al.* 2004; Chandra & Fauchais 2009), liquid atomisation (Ashgriz 2011; Moita & Moreira 2012) and cooling of electronic devices (Pautsch & Shedd 2005; Kim 2007; Sinha-Ray & Yarin 2014; Hsieh & Luo 2016; Breitenbach, Roisman & Tropea 2017; Liang & Mudawar 2017). Of particular importance is the situation in which the surface is heated above the liquid's boiling point. In such case, hydrodynamic behaviours of the impacting droplets, e.g. spreading and possible splashing, are accompanied by various phenomena associated with liquid–vapour phase transition, ranging from bubble nucleation to vigorous boiling (Tran *et al.* 2012; Staat *et al.* 2015; Qiu *et al.* 2016). Intangible physical elements make it challenging to understand and control quantities of practical interest such as the heat dissipation rate from the solid surface (Bhardwaj, Longtin & Attinger 2010; Herbert *et al.* 2013; Jung, Jeong & Kim 2016; Liang *et al.* 2016). In a typical boiling process, two scenarios may happen: (1) the liquid maintains contact with the surface, in which case the heat flux keeps increasing with the surface temperature, and (2) sufficient vapour is generated to completely cover the surface. The former is commonly referred to as the contact boiling regime (Tran *et al.*

† Email address for correspondence: ttran@ntu.edu.sg

2012; Khavari *et al.* 2015), while the latter is known as the Leidenfrost regime (Leidenfrost 1756; van Limbeek *et al.* 2016; Shirota *et al.* 2016; Khavari 2017; Khavari & Tran 2017; Van Limbeek *et al.* 2017; Liu & Tran 2020). In the contact boiling regime, bubbles may be generated at the liquid–solid interface; part of the liquid's spreading area is therefore covered by vapour, and the heat is transferred from the solid to the liquid through both the liquid–solid interface (the wet area) and the generated vapour. As a result, to effectively control the heat transfer rate, one must have a quantitative measure of the wet area during the boiling of the liquid.

In this paper, we accurately and systematically measure the temporal change of the wet area during the impact of ethanol droplets on a heated glass substrate using the total internal reflection (TIR) method (Nagai & Nishio 1996; Kolinski *et al.* 2012; Kolinski, Mahadevan & Rubinstein 2014*a*,*b*; Khavari *et al.* 2015; van Limbeek *et al.* 2016; Shirota *et al.* 2016; Khavari & Tran 2017; Van Limbeek *et al.* 2017). We also report detailed dependence of the measured wet area on impact velocity and surface temperature for various characteristic regimes previously observed for droplet impact on heated surfaces (Khavari *et al.* 2015), i.e. the spreading, bubbly boiling and fingering boiling regimes. We measure the total length of the contact lines during impact and show its variations with surface temperature and impact velocity. We discuss how the formation of fingering patterns contributes to a significant increase in the total length of the contact lines. Furthermore, we present the wetting rate of droplets on heated surfaces for different surface temperatures and impact velocities and discuss its role in distinguishing the bubbly boiling regime from the fingering boiling regime.

2. Results and Discussion

We used the TIR technique (see the Appendix for the experimental setup) to observe and precisely measure the wet area during impact. In particular, we utilised this technique to obtain high-speed recordings in which the wet area is well contrasted from the dry area. This enabled us to precisely measure both the total wet area, denoted by A, and the total length L of the contact lines separating the wet and dry areas. We used ethanol as the working liquid, with density $\rho = 789$ kg m^{-3} and surface tension $\sigma = 22.4 \times 10^{-3}$ N m^{-1}. We kept the droplet diameter fixed at $D_0 = 2$ mm and varied the impact velocity V_0 between 0.34 m s^{-1} and 2.86 m s^{-1} by changing the height of the needle used to dispense droplets. The corresponding range of Weber number, defined as $We = \rho V_0^2 D_0/\sigma$, was from 64 to 591. We used two high-speed cameras to record both side and bottom views of the impact of falling droplets (see Appendix).

Total internal reflection recordings have been used to reveal several distinct impact and boiling behaviours, i.e. spreading, bubbly boiling and fingering boiling, during impact of droplets on a surface heated to temperatures below the Leidenfrost point (Khavari *et al.* 2015). In particular, as the temperature increases from room temperature, the impact behaviour transitions from spreading to bubbly boiling and fingering boiling before finally reaching the Leidenfrost regime. The transition from one boiling regime to another is mainly controlled by the surface temperature (Khavari *et al.* 2015). In each regime, and for a fixed temperature, changing the Weber number leads to substantial variations in the impact dynamics. In figure 1, we show a series of side- and bottom-view snapshots of the impact of ethanol droplets in the fingering boiling regime at $T = 200\,^{\circ}$C and several values of Weber numbers (see supplementary movie 1 available at https://doi.org/10.1017/jfm.2021.745 for a synchronised recording of the side and bottom views of typical impact behaviour in the fingering boiling regime). There are four panels, from

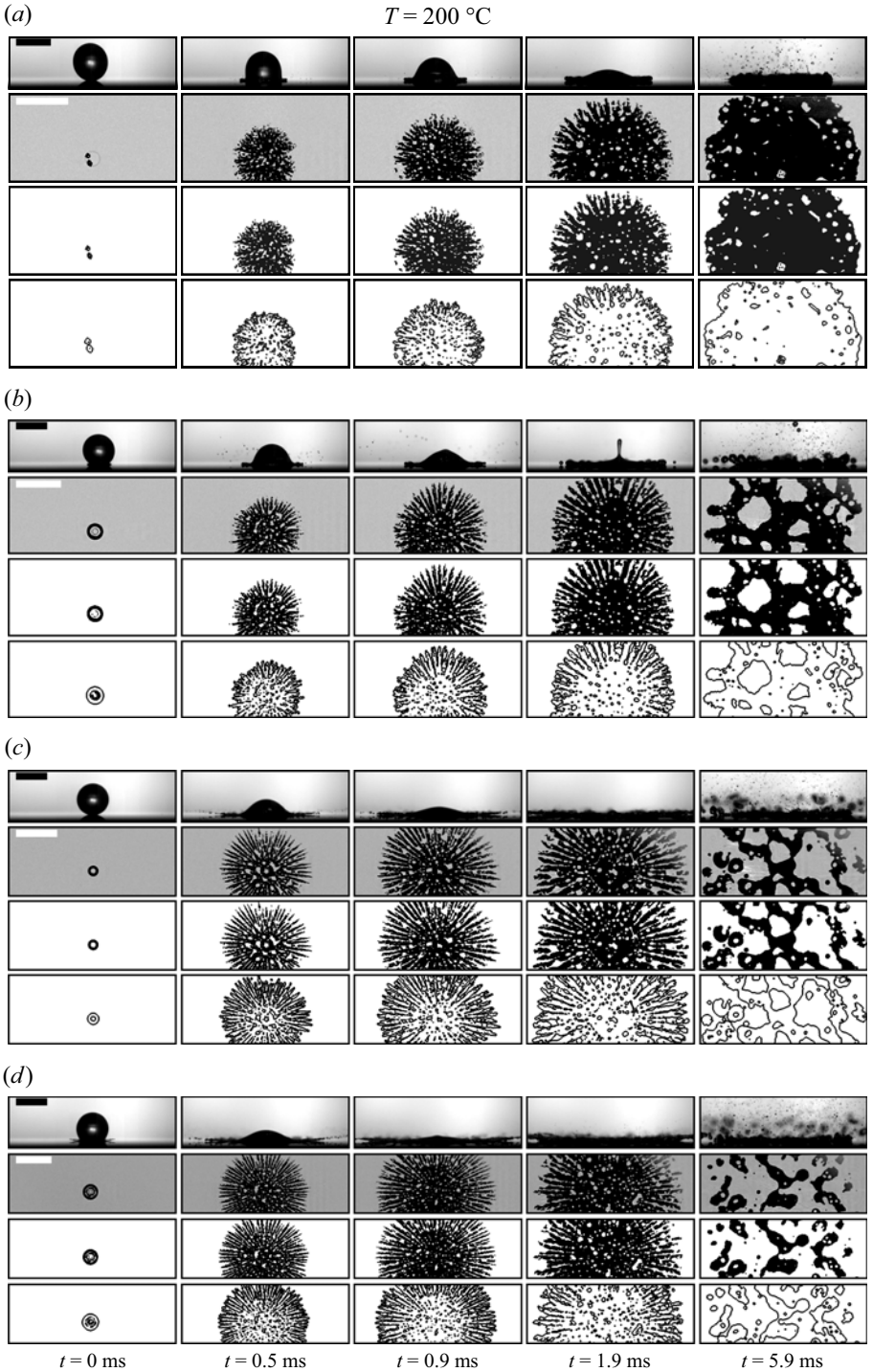

Figure 1. Series of snapshots of impact and boiling behaviours captured at a constant surface temperature ($T = 200\,^{\circ}\mathrm{C}$) and different Weber numbers: (*a*) $We = 64$, (*b*) $We = 130$, (*c*) $We = 372$ and (*d*) $We = 591$. Images in the same column belong to the same time after first contact ($t = 0$ ms). The first row of each panel shows side-view images of impact, while the next three rows display the TIR snapshots and their corresponding binary images of the wet area (third row) and contact lines (fourth row). All the inset scale bars represent the length scale of 2 mm.

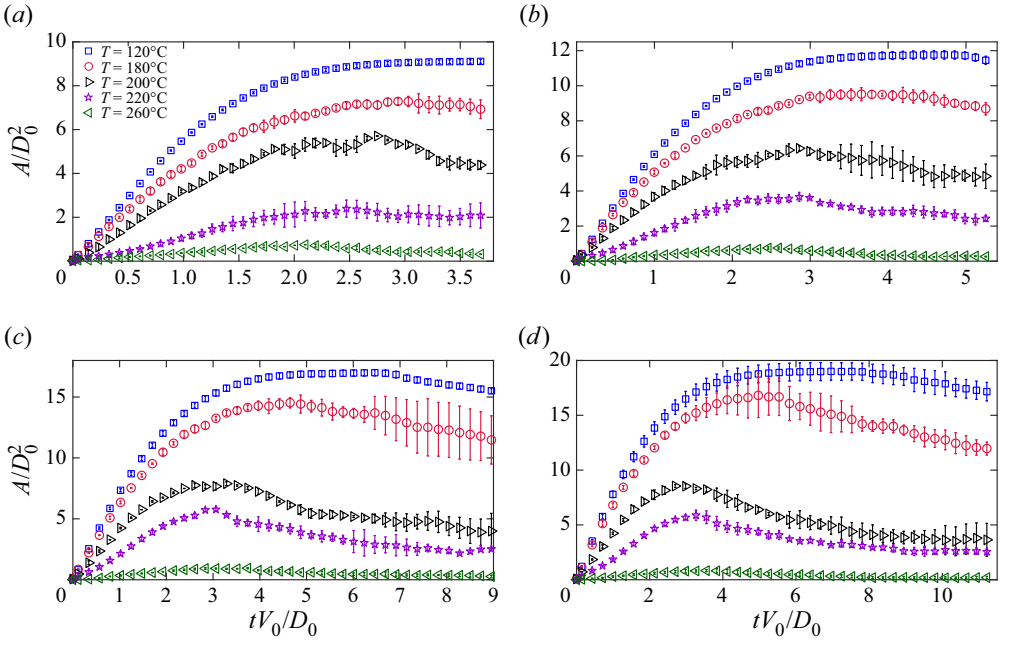

Figure 2. Normalised contact area A/D_0^2 versus normalised time tV_0/D_0 for different surface temperatures: (*a*) $We = 64$, (*b*) $We = 130$, (*c*) $We = 372$ and (*d*) $We = 591$.

figure 1(*a*) to figure 1(*d*), corresponding to four distinct values of Weber number. In each panel, the first row shows a series of side-view snapshots of the impact at several specific times, from the moment of impact, $t = 0$ ms, to $t = 5.9$ ms. The second row shows the corresponding bottom-view snapshots obtained from the TIR recording. The third and fourth rows respectively show the binary images of the wet area and the contact lines extracted from those in the second row. We note that the snapshots in each column were taken at the same time after the impact moment ($t = 0$ ms). The series of snapshots in figure 1 illustrate how the development of fingering patterns, initiated at the temperature $T = 200\,^{\circ}$C, evolves with time and changes with increasing Weber number.

Figure 2 shows the temporal change of the normalised wet area A/D_0^2 for several Weber numbers and surface temperatures. We note that since the field of view of the bottom-view camera is insufficient to capture the entire contact area, we measured the wet area A_s within a sector of central angle α and estimated the total wet area as $A = 2\pi A_s/\alpha$, assuming that the contact area is axisymmetric about the impact point. As a droplet strikes the glass surface, it spreads out radially because of the liquid's inertia: the higher the kinetic energy of the droplet, the larger the wet area. At the same time, the liquid is heated up as soon as it comes in contact with the heated surface. With sufficiently high surface temperature, vapour bubbles are generated at the glass–liquid interface, leading to a range of different physical processes: the bubbles may collapse, merge with neighbouring ones or grow and detach from the surface (see supplementary movie 2 for TIR recordings of the wet area for a fixed Weber number ($We = 591$) and different surface temperatures). As the surface temperature approaches the Leidenfrost temperature, bubble nucleation monotonically increases, driving the system into the bubbly boiling regime and consequently reducing the wet area. This temperature-dependence of A is illustrated by comparing the cases of two different temperatures, $T = 120\,^{\circ}$C and $T = 180\,^{\circ}$C, in figure 2. Thus, the change in

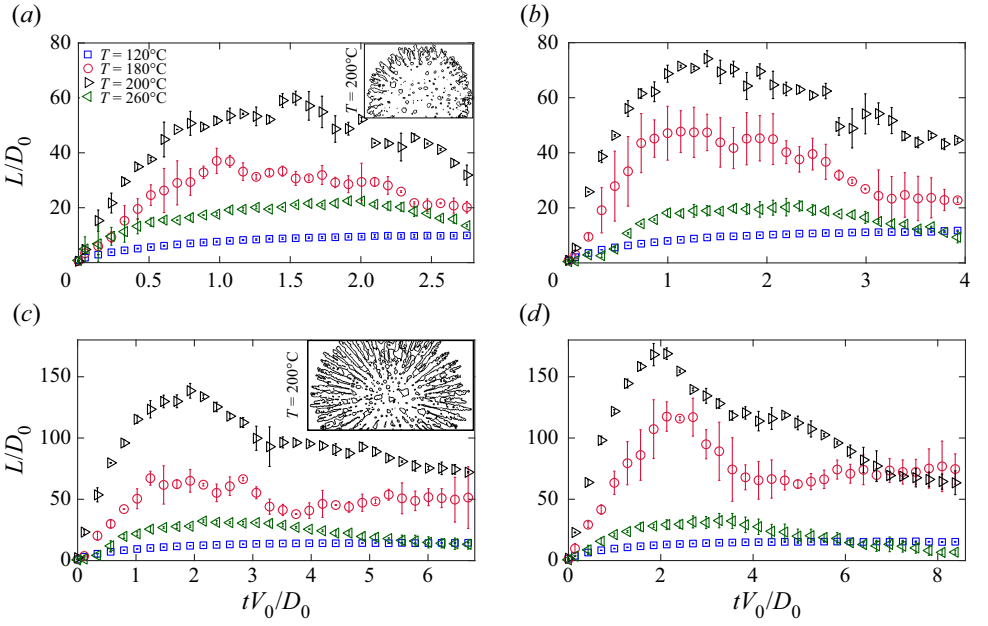

Figure 3. Normalised total length of contact lines L/D_0 versus normalised time tV_0/D_0 for different surface temperatures and Weber numbers: (*a*) $We = 64$, (*b*) $We = 130$, (*c*) $We = 372$ and (*d*) $We = 591$. The inset snapshots of fingering patterns in (*a*,*c*) were taken at $T = 200\,^{\circ}\mathrm{C}$, and their corresponding Weber numbers are $We = 64$ and $We = 372$, respectively. The snapshots show the significant contribution of fingering patterns in increasing the total length of contact lines.

the total wet area results from two competing effects: liquid spreading, which causes A to increase, and boiling, which tends to reduce A.

At $T = 200\,^{\circ}\mathrm{C}$, the wet area takes the shape of a fingering pattern that grows radially as the liquid spreads on the surface (see supplementary movie 3 for TIR recordings of fingering patterns of the same surface temperature, i.e. $T = 220\,^{\circ}\mathrm{C}$, but different Weber numbers). For each tested Weber number, we observe a considerable drop in A compared to that at lower temperatures. The reduction in wet area persists as the surface temperature increases until the system transitions to the Leidenfrost regime, i.e. zero wet area. In our experiments, the Leidenfrost regime is observed at $T \geq 280\,^{\circ}\mathrm{C}$ for $We \leq 130$ and at $T \geq 300\,^{\circ}\mathrm{C}$ for $We \geq 130$.

In figure 3, we show several plots of the normalised total length L/D_0 of contact lines versus the normalised time tV_0/D_0; each plot is obtained for a fixed Weber number and several different temperatures. For all tested Weber numbers, L/D_0 reaches its maximum at $T = 200\,^{\circ}\mathrm{C}$ because of the emergence of fingering patterns. We note that although fingering patterns are still present for $T > 200\,^{\circ}\mathrm{C}$, the number of fingers decreases with further increase in surface temperature. This is the key factor causing the decrease in L for $T > 200$. In figure 3(*a*,*c*), we provide snapshots of the fingering patterns obtained for $T = 200\,^{\circ}\mathrm{C}$ at $t = 1.9$ ms and $t = 0.9$ ms, respectively. The snapshots qualitatively demonstrate how the formation of fingering patterns leads to a significant increase in L while causing a drop in the contact area A (see data corresponding to $T = 200\,^{\circ}\mathrm{C}$ in figure 2). From figure 3, it is worth noting that the dimensionless time at which L/D_0 reaches its maximum is essentially independent of the Weber number; it is also almost independent of the surface temperature for $T > 120\,^{\circ}\mathrm{C}$ (boiling regimes).

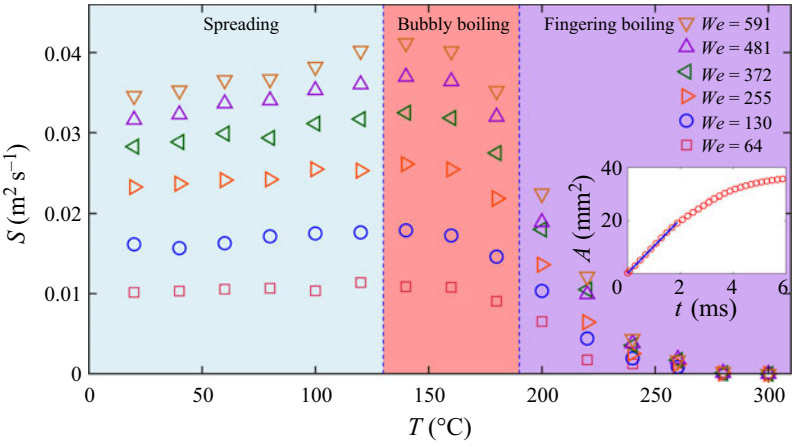

Figure 4. Wetting rate S versus surface temperature T for different Weber numbers. The inset shows a plot of the wet area A versus time t, from which S is calculated as the slope of the best linear fit to the early stage of spreading.

We now examine how fast the liquid wets the heated surface and how the wetting rate depends on the surface temperature and the Weber number. To this end, we determine the wetting rate $S = \mathrm{d}A/\mathrm{d}t$ at the initial moments of impact. In figure 4, we show the plot of S versus T for different Weber numbers across all the observed regimes. We note that, for clarity, the error bars are not shown in this plot. The inset of figure 4 shows a respresentative plot of A versus t from which S is extracted. We observe from figure 4 that S weakly depends on T for a wide range of surface temperatures in the spreading and bubbly boiling regimes, However, the wetting rate shows a strong dependence on the Weber number. The most crucial observation is that the wetting rate decreases sharply as soon as fingering formation emerges. This sets a clear distinction between the bubbly boiling and the fingering boiling regimes. The drop in S at the transition between the bubbly and the fingering boiling regimes is also consistent with the sharp drop in the wet area associated with the formation of fingering patterns.

In conclusion, we have reported accurate measurements of the contact area as well as the total length of contact lines during the impact of ethanol droplets on a heated glass surface. Using the TIR technique combined with high-speed imaging, we obtained real-time reduction in the wet area when the bubble nucleation initiated. We also showed how formation of fingering patterns contributed to the increase of the total length of contact lines. Finally, we showed that the initial wetting rate is insensitive to temperature change in the spreading and bubbly boiling regimes, but exhibits a substantial drop when the impact behaviour transitions from bubbly boiling to fingering boiling.

Supplementary movies. Supplementary movies are available at https://doi.org/10.1017/jfm.2021.745.

Funding. This work was supported by the Nanyang Technological University (NTU) and Ministry of Education (MOE, grant number MOE2018-T2-2-113), Singapore.

Declaration of interests. The authors report no conflict of interest.

Author ORCIDs.
Mohammad Khavari https://orcid.org/0000-0003-1972-2970;
Tuan Tran https://orcid.org/0000-0002-5132-6495.

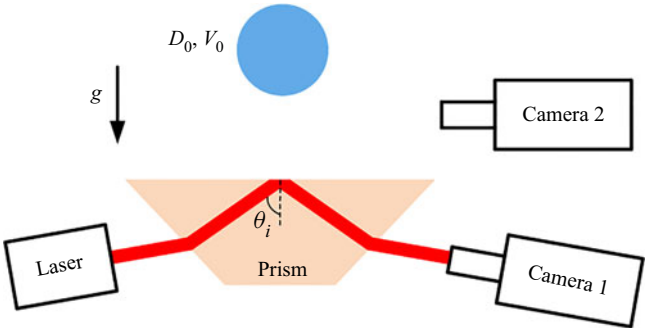

Figure 5. Experimental setup for TIR measurements. The incident angle θ_i is required to satisfy the TIR condition. Camera 1 captures the TIR signal at the top surface of the glass prism, i.e. the bottom view of the impact and boiling behaviours, while camera 2 records the impact from the side.

Appendix. Experimental setup

A schematic of our experimental setup is shown in figure 5. To satisfy the required conditions for TIR at the glass–air interface, we illuminate a red laser ($\lambda = 640$ nm) through a glass Dove prism (N-BK7, Thorlabs Inc.) using a beam expander and mirrors. The light directed towards the top surface of the glass prism has an incident angle of θ_i satisfying the TIR condition $\theta_{sa} < \theta_i < \theta_{sl}$, where θ_{sa} and θ_{sl} are the critical angles at the glass–air and the glass–liquid interfaces, respectively.

The TIR condition ensures that incident light is totally reflected from the glass–air interface (dry areas), while it is refracted into the liquid at the glass–liquid interface (wet areas). In recorded images, the dry areas appear bright and wet areas appear dark. We use two high-speed cameras to record the impact dynamics. Camera 1 (SA-X2, Photron Inc.) is used to record the bottom view, and camera 2 (APX-RS, Photron Inc.) is used to record the side view. The impact velocity (V_0) and drop size (D_0) of each impact experiment are also obtained from the side-view recording.

References

Ashgriz, N. 2011 *Handbook of Atomization and Sprays: Theory and Applications*. Springer Science & Business Media.

Bhardwaj, R., Longtin, J.P. & Attinger, D. 2010 Interfacial temperature measurements, high-speed visualization and finite-element simulations of droplet impact and evaporation on a solid surface. *Intl J. Heat Mass Transfer* **53** (19), 3733–3744.

Breitenbach, J., Roisman, I.V. & Tropea, C. 2017 Heat transfer in the film boiling regime: single drop impact and spray cooling. *Intl J. Heat Mass Transfer* **110**, 34–42.

Chandra, S. & Fauchais, P. 2009 Formation of solid splats during thermal spray deposition. *J. Therm. Spray Technol.* **18** (2), 148–180.

Davis, J.R., *et al.* 2004 *Handbook of Thermal Spray Technology*. ASM International.

Herbert, S., Fischer, S., Gambaryan-Roisman, T. & Stephan, P. 2013 Local heat transfer and phase change phenomena during single drop impingement on a hot surface. *Intl J. Heat Mass Transfer* **61**, 605–614.

Hsieh, S.-S. & Luo, S.-Y. 2016 Droplet impact dynamics and transient heat transfer of a micro spray system for power electronics devices. *Intl J. Heat Mass Transfer* **92**, 190–205.

Jung, J., Jeong, S. & Kim, H. 2016 Investigation of single-droplet/wall collision heat transfer characteristics using infrared thermometry. *Intl J. Heat Mass Transfer* **92**, 774–783.

Khavari, M. 2017 Droplet impact on superheated surfaces. PhD thesis, Nanyang Technological University.

Khavari, M., Sun, C., Lohse, D. & Tran, T. 2015 Fingering patterns during droplet impact on heated surfaces. *Soft Matt.* **11** (17), 3298–3303.

KHAVARI, M. & TRAN, T. 2017 Universality of oscillating boiling in leidenfrost transition. *Phys. Rev.* E **96**, 043102.

KIM, J. 2007 Spray cooling heat transfer: the state of the art. *Intl J. Heat Fluid Flow* **28** (4), 753–767.

KOLINSKI, J.M., MAHADEVAN, L. & RUBINSTEIN, S.M. 2014*a* Drops can bounce from perfectly hydrophilic surfaces. *Europhys. Lett.* **108** (2), 24001.

KOLINSKI, J.M., MAHADEVAN, L. & RUBINSTEIN, S.M. 2014*b* Lift-off instability during the impact of a drop on a solid surface. *Phys. Rev. Lett.* **112** (13), 134501.

KOLINSKI, J.M., RUBINSTEIN, S.M., MANDRE, S., BRENNER, M.P., WEITZ, D.A. & MAHADEVAN, L. 2012 Skating on a film of air: drops impacting on a surface. *Phys. Rev. Lett.* **108** (7), 074503.

LEIDENFROST, J.G. 1756 De aquae communis nonnullis qualitatibus tractatus. Duisburg translation: on the fixation of water in diverse fire. *Intl J. Heat Mass Transfer* **9**, 1153–1166 (1966).

LIANG, G., MU, X., GUO, Y., SHEN, S., QUAN, S. & ZHANG, J. 2016 Contact vaporization of an impacting drop on heated surfaces. *Exp. Therm. Fluid Sci.* **74**, 73–80.

LIANG, G. & MUDAWAR, I. 2017 Review of drop impact on heated walls. *Intl J. Heat Mass Transfer* **106**, 103–126.

VAN LIMBEEK, M.A.J., SHIROTA, M., SLEUTEL, P., SUN, C., PROSPERETTI, A. & LOHSE, D. 2016 Vapour cooling of poorly conducting hot substrates increases the dynamic leidenfrost temperature. *Intl J. Heat Mass Transfer* **97**, 101–109.

LIU, D. & TRAN, T. 2020 Size-dependent spontaneous oscillations of leidenfrost droplets. *J. Fluid Mech.* **902**, A21.

MOITA, A.S. & MOREIRA, A.L.N. 2012 Scaling the effects of surface topography in the secondary atomization resulting from droplet/wall interactions. *Exp. Fluids* **52** (3), 679–695.

NAGAI, N. & NISHIO, S. 1996 Leidenfrost temperature on an extremely smooth surface. *Exp. Therm. Fluid Sci.* **12** (3), 373–379.

PAUTSCH, A.G. & SHEDD, T.A. 2005 Spray impingement cooling with single-and multiple-nozzle arrays. Part I: heat transfer data using fc-72. *Intl J. Heat Mass Transfer* **48** (15), 3167–3175.

QIU, L., DUBEY, S., CHOO, F.H. & DUAN, F. 2016 The transitions of time-independent spreading diameter and splashing angle when a droplet train impinging onto a hot surface. *RSC Adv.* **6** (17), 13644–13652.

SHIROTA, M., VAN LIMBEEK, M.A.J., SUN, C., PROSPERETTI, A. & LOHSE, D. 2016 Dynamic leidenfrost effect: relevant time and length scales. *Phys. Rev. Lett.* **116** (6), 064501.

SINHA-RAY, S. & YARIN, A.L. 2014 Drop impact cooling enhancement on nano-textured surfaces. Part I: theory and results of the ground (1g) experiments. *Intl J. Heat Mass Transfer* **70**, 1095–1106.

STAAT, H.J.J., TRAN, T., GEERDINK, B., RIBOUX, G., SUN, C., GORDILLO, J.M. & LOHSE, D. 2015 Phase diagram for droplet impact on superheated surfaces. *J. Fluid Mech.* **779**, R3.

TRAN, T., STAAT, H.J.J., PROSPERETTI, A., SUN, C. & LOHSE, D. 2012 Drop impact on superheated surfaces. *Phys. Rev. Lett.* **108** (3), 036101.

VAN LIMBEEK, M.A.J., SCHAARSBERG, M.H.K., SOBAC, B., REDNIKOV, A., SUN, C., COLINET, P. & LOHSE, D. 2017 Leidenfrost drops cooling surfaces: theory and interferometric measurement. *J. Fluid Mech.* **827**, 614–639.